The Astrophysical Journal, 882:4 (14pp), 2019 September 1 https://doi.org/10.3847/1538-4357/ab322b
© 2019. The American Astronomical Society. All rights reserved.

The Sloan Digital Sky Survey Reverberation Mapping Project: Low-ionization Broad-line Widths and Implications for Virial Black Hole Mass Estimation

Shu Wang[1,2], Yue Shen[3,4,11], Linhua Jiang[1,2], Keith Horne[5], W. N. Brandt[6,7,8], C. J. Grier[6,9], Luis C. Ho[1,2], Yasaman Homayouni[10], Jennifer I-Hsiu Li[3], Donald P. Schneider[6,7], and Jonathan R. Trump[10]

[1] Kavli Institute for Astronomy and Astrophysics, Peking University, Beijing 100871, People's Republic of China; wangshukiaa@pku.edu.cn, jiangKIAA@pku.edu.cn
[2] Department of Astronomy, School of Physics, Peking University, Beijing 100871, People's Republic of China
[3] Department of Astronomy, University of Illinois at Urbana-Champaign, Urbana, IL 61801, USA
[4] National Center for Supercomputing Applications, University of Illinois at Urbana-Champaign, Urbana, IL 61801, USA
[5] SUPA Physics and Astronomy, University of St. Andrews, Fife, KY16 9SS, Scotland, UK
[6] Department of Astronomy & Astrophysics, The Pennsylvania State University, University Park, PA 16802, USA
[7] Institute for Gravitation and the Cosmos, The Pennsylvania State University, University Park, PA 16802, USA
[8] Department of Physics, 104 Davey Lab, The Pennsylvania State University, University Park, PA 16802, USA
[9] Steward Observatory, University of Arizona, 933 North Cherry Avenue, Tucson, AZ 85721-0065, USA
[10] University of Connecticut, Department of Physics, 2152 Hillside Road, Unit 3046, Storrs, CT 06269-3046, USA
Received 2019 March 24; revised 2019 June 22; accepted 2019 July 6; published 2019 August 26

Abstract

The width of the broad emission lines in quasars is commonly characterized by either the FWHM or the square root of the second moment of the line profile ($\sigma_{\rm line}$) and used as an indicator of the virial velocity of the broad-line region (BLR) in the estimation of black hole (BH) mass. We measure FWHM and $\sigma_{\rm line}$ for Hα, Hβ, and Mg II broad lines in both the mean and rms spectra of a large sample of quasars from the Sloan Digital Sky Survey Reverberation Mapping project. We introduce a new quantitative recipe to measure $\sigma_{\rm line}$ that is reproducible, is less susceptible to noise and blending in the wings, and scales with the intrinsic width of the line. We compare the four definitions of line width (FWHM and $\sigma_{\rm line}$ in mean and rms spectra, respectively) for each of the three broad lines and among different lines. There are strong correlations among different width definitions for each line, providing justification for using the line width measured in single-epoch spectroscopy as a virial velocity indicator. There are also strong correlations among different lines, suggesting that alternative lines to Hβ can be used to estimate virial BH masses. We further investigate the correlations between virial BH masses using different line width definitions and the stellar velocity dispersion of the host galaxies and the dependence of line shape (characterized by the ratio FWHM/$\sigma_{\rm line}$) on physical properties of the quasar. Our results provide further evidence that FWHM is more sensitive to the orientation of a flattened BLR geometry than $\sigma_{\rm line}$, but the overall comparison between the virial BH mass and host stellar velocity dispersion does not provide conclusive evidence that one particular width definition is significantly better than the others.

Key words: black hole physics – galaxies: active – line: profiles – quasars: general – surveys

Supporting material: FITS file

1. Introduction

Measuring black hole (BH) masses in quasars is of critical importance to most studies of supermassive BHs. The primary method to measure BH masses is the reverberation mapping (RM; e.g., Blandford & McKee 1982; Peterson 1993), where the time lag τ between the continuum and broad emission line variability provides a measurement of the characteristic size of the broad-line region (BLR), i.e., $R = c\tau$. Assuming that the BLR is virialized, a virial BH mass can be computed using the broad-line velocity width W as an indicator of the virial velocity: $M_{\rm BH} = f\frac{W^2R}{G}$, where f is the dimensionless virial coefficient that accounts for the geometry and kinematics of the BLR. Local RM results have discovered a remarkable correlation between the size of the BLR and the luminosity of the active galactic nucleus (AGN), known as the R–L relation (e.g., Kaspi et al. 2000; Bentz et al. 2013), which was subsequently utilized to develop the single-epoch virial BH mass estimators that allow the estimation of a BH mass using a single spectrum (e.g., Vestergaard & Peterson 2006; Shen 2013).

The only directly measured quantity used in the virial BH mass estimation is the width of the broad line. There are two commonly used characterizations of line width (e.g., Peterson et al. 2004), the FWHM and the square root of the second moment of the line (referred to as the line dispersion $\sigma_{\rm line}$). For single-epoch spectroscopy, both FWHM and $\sigma_{\rm line}$ are measured from the spectrum. However, for objects with reverberation mapping spectroscopy, both line widths can also be measured from the rms spectrum, which better represents the variable component of the line. Although there are correlations between these different line width definitions (e.g., Collin et al. 2006, hereafter C06), it remains a topic of debate as to which line width definition is better to indicate the virial velocity of the BLR. The pros and cons of these different line width definitions have been discussed at length in, e.g., Peterson et al. (2004) and Peterson (2011). From a practical point of view, FWHM is relatively easier to measure and less susceptible to blending and noisy wings of the line than $\sigma_{\rm line}$ (e.g., Peterson et al. 2004); however, FWHM is more sensitive to inappropriate narrow-line removal and may be more affected by orientation in a flattened

[11] Alfred P. Sloan Research Fellow.

geometry of the BLR than $\sigma_{\rm line}$ (e.g., Wills & Browne 1986; Runnoe et al. 2013; Shen & Ho 2014; Brotherton et al. 2015; Mejía-Restrepo et al. 2018). On the other hand, there may be systematic differences in the line widths measured from the mean and rms spectra.

C06 performed the first systematic comparison among the four types of line width measurements (FWHM and $\sigma_{\rm line}$ from both mean and rms spectra) using 35 low-redshift AGNs with RM measurements. By comparing the virial products based on the four different width measurements with the stellar velocity dispersion (used as an independent indicator of the true BH mass via the $M_{\rm BH}$–σ_* relation; e.g., Tremaine et al. 2002) of 14 host galaxies, they concluded that $\sigma_{\rm line}$ is a better indicator of the virial velocity than FWHM, as the latter displayed a larger variation of the virial coefficient f across subpopulations of objects.

In this work we expand the C06 with a new RM sample from the Sloan Digital Sky Survey Reverberation Mapping (SDSS-RM) project (Shen et al. 2015a). Our sample is the largest to date with which one can measure all four types of broad-line widths for multiple broad lines. In Section 2 we describe the sample and the data used, and in Section 3 we detail our methodology for obtaining line width measurements. We present our main results in Section 4, discuss their significance in Section 5, and conclude in Section 6 with a discussion on future perspectives.

2. Data and Sample

SDSS-RM is a dedicated RM project that uses the SDSS BOSS spectrograph (Smee et al. 2013) on the 2.5 m SDSS telescope (Gunn et al. 2006) to monitor 849 broad-line quasars in a single 7 deg^2 field over a broad redshift and luminosity range (Shen et al. 2015a). The SDSS-RM sample is a flux-limited sample and is designed to be a representative sample of the general quasar population without any cuts on spectral and variability properties of quasars. A detailed description of the sample characterization is presented in Shen et al. (2019). From the commencement of this program as part of SDSS-III (Eisenstein et al. 2011), SDSS-RM obtained 32 spectroscopic epochs in 2014 at an average cadence of ∼4 days and will continue through 2020 with 6–12 spectroscopic epochs per observing season.

The spectroscopic data used in this work are the 32 epochs taken during 2014. Both the individual epoch spectra and the co-added spectra during this period are used in our analysis. The wavelength coverage of BOSS spectrographs is ∼3650–10400 Å, with a spectral resolution of $R \sim 2000$. The spectroscopic data are first pipeline-processed as part of the SDSS-III Data Release 12 (Alam et al. 2015), followed by a custom flux calibration scheme and improved sky subtraction as described in Shen et al. (2015a). The improved spectrophotometry has a nominal accuracy of 5%.

In order to improve further the flux calibration and to construct rms spectra from the first-year data, we use a custom program called "PrepSpec" developed by K. Horne. As detailed in Shen et al. (2016), PrepSpec models the time-resolved spectroscopic data set with a separable model that accounts for the variations in the broad-line and continuum flux. During this process, the fluxes of the narrow emission lines, assumed to be constant during the monitoring period, are used to adjust and improve the overall flux calibration. PrepSpec measures the continuum and broad-line fluxes as time series from the model and generates the rms spectra for the major broad emission lines. This approach differs from earlier RM work (e.g., Peterson et al. 2004); the construction of the rms spectra isolates the continuum variability from the broad-line variability and traces the variability in the broad lines. PrepSpec employs rigorous statistical modeling (assuming Gaussian errors) to create the light curves (continuum and broad-line variability) and the rms line profile along with their measurement uncertainties. These rms broad-line spectra are used to measure the broad-line widths in our study.

3. Line Width Measurement

This work compares the two commonly adopted line width definitions, FWHM and $\sigma_{\rm line}$, for different broad lines. Since both FWHM and $\sigma_{\rm line}$ can be measured from the mean and rms spectra, we consider four different line width measurements: FWHM$_{\rm mean}$, FWHM$_{\rm rms}$, $\sigma_{\rm line,mean}$, and $\sigma_{\rm line,rms}$.

3.1. Mean and rms Spectra

The mean spectra are constructed by co-adding all 32 epochs for each of the 849 quasars in the SDSS-RM sample using the SDSS-III spectroscopic pipeline idlspec2d.[12] These co-added spectra are nearly identical to those generated with a simple arithmetic mean or inverse-variance-weighted mean; therefore, this detail does not significantly affect the measurements of the broad-line widths. PrepSpec also outputs a mean spectrum for each quasar that is essentially the same as our own co-added spectrum.

There are two approaches to construct the rms broad-line spectrum. The commonly used method (e.g., Peterson et al. 2004) is to directly compute the rms value, pixel by pixel, over all epochs for the total spectral flux (continuum plus lines); the rms line profile is obtained by subtracting the local continuum in the total rms spectrum. The second approach is to subtract the continuum in each epoch and compute the rms from the line-only spectra. As noted by Barth et al. (2015), there are systematic differences between the line-only rms spectra from these two approaches. Appendix A provides our simulations to demonstrate such differences. The main reason that earlier RM studies adopted the former approach is that it is relatively straightforward to compute and does not rely on specific modeling of the decomposition of continuum and line flux, although the resultant rms line spectrum generated is a biased measure of the true line variability. PrepSpec generates the rms line spectrum following the second approach, where the rms variability is from the broad emission line only.

3.2. Spectral Fitting of the Mean Spectrum

The multicomponent functional fitting method is used to decompose the mean spectra following our earlier work (e.g., Shen et al. 2008, 2011). We use the publicly available code `QSOFIT` (Shen et al. 2019) with small modifications to perform our spectral fits. Examples of our fitting result are displayed in Figure 1. Compared with direct pixel measurement from the original spectrum, this approach is more robust against noise and artifacts in the reduction process. To confirm that the model accurately reproduces the data, we visually inspect all the fitting results and reject poorly fit objects from

[12] Publicly available at http://www.sdss3.org/svn/repo/idlspec2d/.

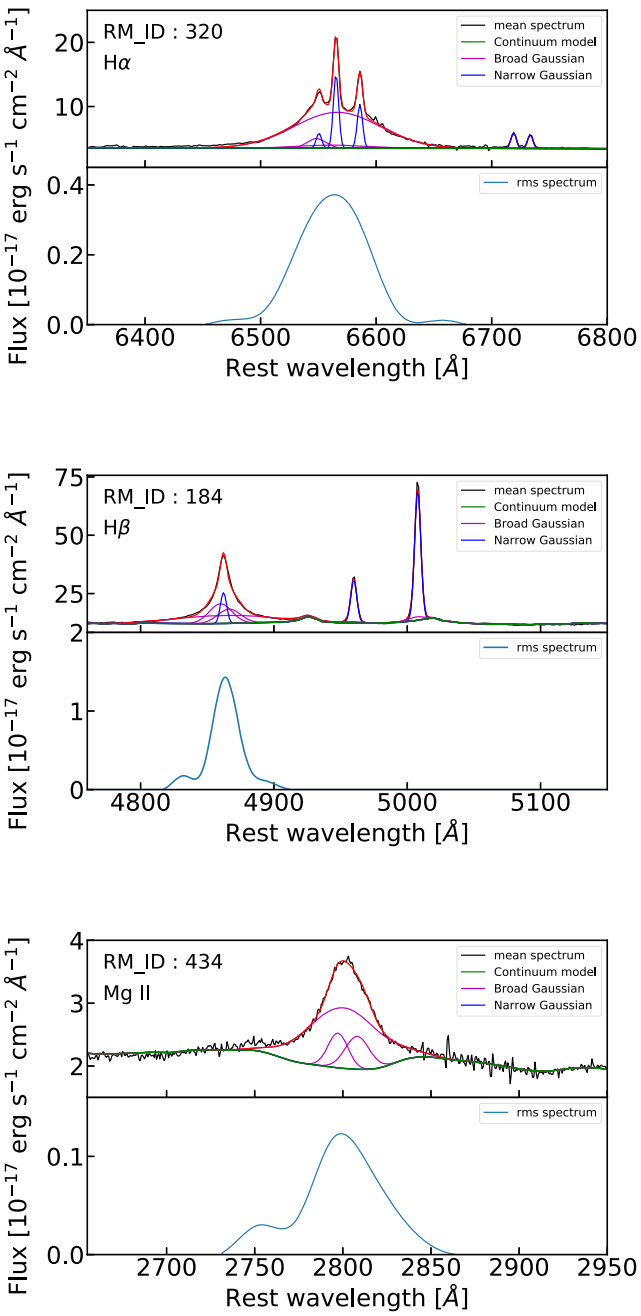

Figure 1. Examples of line-fitting results from the mean and rms spectra for Hα, Hβ, and Mg II from top to bottom, respectively. The RMID of each object is shown in the upper left corner. Black lines are the mean spectra. Green lines are the continuum model, which is the sum of the power-law component, Fe II emission, and the polynomial component (for Mg II only). Magenta and blue lines indicate each of the broad and narrow Gaussian components, respectively. Red lines represent the total line model. All line-fitting results in the figure are calculated by adding the underlying continuum model to match the mean spectrum. The rms spectrum from PrepSpec is shown in the bottom of each panel as the blue line.

later analysis. Rejection using a cut on the reduced χ^2 statistic results in a similar subsample to our visual inspection.

In this work, we focus on three broad emission lines: Hα, Hβ, and Mg II. These lines are covered in the low-redshift and low-luminosity subset of the SDSS-RM sample, and therefore their variations are well captured by the 2014 spectroscopy. High-ionization lines, such as C IV, are present in the high-redshift subset of the SDSS-RM sample. The 2014 data do not cover a sufficient time baseline to probe the C IV variability for most objects in our sample. An extension of the current work to C IV and other broad lines covered in the high-z SDSS-RM subsample will be presented in future work using the final multiyear SDSS-RM data set.

Table 1
Line-fitting Parameters

Line	Rest Wavelength[a] (Å)	$N_{\rm Gauss}$	Complex
Hα	6564.61	4[b]	Hα
[S II]	6732.67	1	Hα
[S II]	6718.29	1	Hα
[N II]	6549.85	1	Hα
[N II]	6585.28	1	Hα
Hβ	4862.68	4[b]	Hβ
[O III]	4960.30	2	Hβ
[O III]	5008.24	2	Hβ
Mg II	2798.75	4[b]	Mg II

Notes.
[a] The rest wavelengths are in vacuum.
[b] Three Gaussians are used to fit the broad-line component, and one Gaussian is used for the narrow-line component.

We first fit the continuum and broadband Fe II emission near the broad emission line of interest and subtract the pseudo-continuum (continuum plus Fe II emission) from the spectrum, leaving a line-only residual spectrum (see below). Each broad line in the residual spectrum is fit using multiple Gaussians. We chose to fit each line locally to avoid complex continuum shapes over broad spectral ranges. In the regions adjacent to either Hα or Hβ, emission lines existing within each line complex are fit simultaneously with Gaussian functions. Table 1 lists the names, central wavelengths, and number of Gaussians for each line component in the fits.

To fit the local continuum, we choose windows that are free of prominent emission or absorption lines. The specific continuum windows for each line complex are described below. The continuum model consists of a power law and Fe II emission constrained from templates. In the continuum fitting of Mg II, a low-order polynomial in λ is added in order to account for possible reddening in the rest-frame UV regime. The Fe II emission is modeled using templates from Boroson & Green (1992) in the optical and from Vestergaard & Wilkes (2001) in the UV.

To fit each line complex, we transform the spectrum into velocity space using the vacuum wavelength of the line and the redshift of the quasar. As shown in Table 1, the broad lines are fit with three Gaussians and the narrow lines are fit with one Gaussian in each complex. The only exception is [O III] $\lambda\lambda$4959, 5007, where one additional Gaussian is added to account for the blue asymmetric wing (e.g., Peterson et al. 1981; Shen & Ho 2014). The broad- and narrow-line division is set to be 400 km s^{-1} in Gaussian σ, which is $\sim$940 km s^{-1} in FWHM. This division works well for Hα and Hβ in all objects in our sample. During the fitting, all narrow-line centers and widths are tied together in each line complex, and the flux ratios of the doublets are set to their theoretical values. In most cases, the initial estimate of the line center is set to zero velocity. The initial width of the narrow lines is set to $\sigma = 250$ km s^{-1}, while the initial width of the broad lines is set to $\sigma = 650$ km s^{-1} for two Gaussians and 1500 km s^{-1} for the third Gaussian.

The specific fitting details for each line complex are as follows:

1. Hα: The continuum windows are [6150, 6250] Å and [6800, 7000] Å. After subtracting the continuum model, the [S II] $\lambda\lambda$6718, 6732 doublet is fitted. The reason for this step is to obtain a prior on the center and especially the width of the narrow lines to help decompose the narrow Hα component more accurately. The [S II] doublet is fitted using three Gaussians, two for the doublet and one additional Gaussian as an approximation of the red wing of broad Hα. All lines in the complex are fitted simultaneously, including broad and narrow Hα, the [N II] $\lambda\lambda$6549, 6585 doublet, and the [S II] $\lambda\lambda$6718, 6732 doublet. If the fit of [S II] is acceptable (i.e., reduced χ^2 less than 10), the values of line centers and widths for all narrow-line components (narrow Hα, [N II] $\lambda\lambda$6549, 6585) are tied to the values of [S II]. If the [S II] fit has a reduced χ^2 greater than 10, the initial values of all narrow lines are set as the value described above. Our spectra generally have very high signal-to-noise ratio (S/N) per pixel; hence, our Gaussian fit may not be a good fit to the [S II] line in a statistical sense. Therefore, we use a moderately large reduced χ^2 cut to exclude obviously bad [S II] fits. The line flux ratio of the [S II] doublet is fixed to 1, and that of [N II] λ6585 to [N II] λ6549 is fixed to 3.
2. Hβ: The continuum windows are [4450, 4630] Å, [4750, 4770] Å, and [5050, 5500] Å. These windows are chosen to avoid contamination by Hγ and He II λ4686. After subtracting the continuum model, all lines are simultaneously fitted, including broad and narrow Hβ, as well as the [O III] doublet. Each line in the [O III] doublet is fitted with two Gaussians, one for the core component and the other for the blueshifted wing component. For the wing Gaussian, the initial center is set to 200 km s^{-1} blueward of the [O III] vacuum wavelength, and the initial σ of the Gaussian is set to 510 km s^{-1}. The flux ratio of the [O III] doublet is not constrained to allow better fitting for strong [O III] lines.
3. Mg II: The continuum windows are [2300, 2700] Å and [2900, 3400] Å. An additional third-order polynomial in λ is added to account for possible reddening seen in some objects (e.g., Shen et al. 2019). In the line fitting, Mg II is not treated as a doublet because the line is generally too broad to separate the doublet. The initial estimates and limits on the fitting parameters are set as the fiducial values described above.

3.3. Line Width Measurements

While PrepSpec also outputs broad-line widths from the mean and rms spectra, we decided to perform our own measurements. This is because the current version of PrepSpec does not perform a spectral decomposition in the mean spectrum as sophisticated as our approach described above and some line widths reported by PrepSpec are biased. In addition, we will also investigate different choices of windows in measuring $\sigma_{\rm line}$, requiring our own analysis. Visual inspection of the spectral modeling and line width measurements for individual objects suggests that our own line width measurements are generally more reliable than the default PrepSpec outputs.

The sum of all broad Gaussians in our spectral decomposition of the mean spectrum is used to measure FWHM$_{\rm mean}$ and $\sigma_{\rm line,mean}$, and the rms model spectra from PrepSpec are used for the measurements of FWHM$_{\rm rms}$ and $\sigma_{\rm line,rms}$.

Table 2
Number of Objects in Each Subsample

	Total	Good Mean	Good rms	Good Mean and rms[a]
Hα	58	45	39	38
Hβ	222	170	81	76
Mg II	755	512	329	296
Hα & Hβ	58	43	31	⋯
Mg II & Hβ	204	114	43	⋯

Note.
[a] The numbers of the good mean and rms sample for Hα & Hβ and Mg II & Hβ are not shown since we did not use such samples in our study.

To measure FWHM, we first locate the peak of the line model and then identify the half-peak positions on both the red and blue sides of the peak, $\lambda_{\rm redhalf}$ and $\lambda_{\rm bluehalf}$. The FWHM is calculated as

$$\mathrm{FWHM} = \lambda_{\rm redhalf} - \lambda_{\rm bluehalf}. \quad (1)$$

$\sigma_{\rm line}$ is calculated from its definition (e.g., Peterson et al. 2004):

$$\sigma_{\rm line}^2 = \langle\lambda^2\rangle - \lambda_0^2 = \left(\int \lambda^2 F(\lambda) d\lambda\right) \Big/ \left(\int F(\lambda) d\lambda\right) - \lambda_0^2, \quad (2)$$

where $F(\lambda)$ is the line profile and λ_0 is the first moment of $F(\lambda)$,

$$\lambda_0 = \left(\int \lambda F(\lambda) d\lambda\right) \Big/ \left(\int F(\lambda) d\lambda\right). \quad (3)$$

After that, we convert FWHM and $\sigma_{\rm line}$ to velocity units.

In Equation (2) the integrand in the first term is proportional to λ^2, which means that the $\sigma_{\rm line}$ measurement is sensitive to window choices. Ideally the integration in Equation (2) should be over the entire wavelength range of the broad line. However, in practice this approach is not possible because the broad-line profile is typically poorly constrained in the wings owing to the limited S/N of the spectrum. To make our $\sigma_{\rm line}$ measurement repeatable, we define a window that can be easily computed for any spectrum. We tested using multiples of FWHM$_{\rm mean}$ and MAD$_{\rm mean}$ (the Mean Absolute Deviation) as the window. MAD is defined as

$$\mathrm{MAD} = \left(\int |\lambda - \ \mathrm{MED}\ | \ F(\lambda) d\lambda\right) \Big/ \left(\int F(\lambda) d\lambda\right), \quad (4)$$

where MED is the median wavelength of the line profile and is defined as the location where the integrated flux (weight) from the blue side to this location is half of the total line flux.

We finally adopt 2.5 × MAD$_{\rm mean}$ as the *half-window size* to calculate $\sigma_{\rm line}$ for both mean and rms spectra. For mean spectra, the window is centered at the vacuum wavelength of the line. For rms spectra the line center is redefined as the peak of the rms profile in order to enclose much of the rms flux, since the rms profile can be significantly asymmetric. This choice of a MAD$_{\rm mean}$-based window has several advantages: it is a well-defined window that can be reproduced in other work; MAD itself is a measure of the line width, so the window is automatically adjusted according to line width; and using such a window to calculate $\sigma_{\rm line}$ mitigates noise or artifacts in the wings of the line, as well as contamination from residuals from

Table 3
Line Width Measurements

Column No.	Column Name	Type	Units	Description
0	RMID	INT	⋯	SDSS-RM identification number
1	SDSS name	STRING	⋯	Name of the object in SDSS
2	RA	DOUBLE	deg	R.A. (J2000)
3	DEC	DOUBLE	deg	Decl. (J2000)
4	Redshift	DOUBLE	⋯	Redshift
5	SIGMA_HOST	DOUBLE[2]	km s^{-1}	Stellar velocity dispersion and its measurement uncertainty
6	HALPHA_FWHM_mean	DOUBLE[2]	km s^{-1}	Hα FWHM (and measurement uncertainty) in mean spectra
7	HALPHA_SIGMA_mean	DOUBLE[2]	km s^{-1}	Hα $\sigma_{\rm line}$ (and measurement uncertainty) in mean spectra
8	HALPHA_FWHM_rms	DOUBLE[2]	km s^{-1}	Hα FWHM (and measurement uncertainty) in rms spectra
9	HALPHA_SIGMA_rms	DOUBLE[2]	km s^{-1}	Hα $\sigma_{\rm line}$ (and measurement uncertainty) in rms spectra
10	HBETA_FWHM_mean	DOUBLE[2]	km s^{-1}	Hβ FWHM (and measurement uncertainty) in mean spectra
11	HBETA_SIGMA_mean	DOUBLE[2]	km s^{-1}	Hβ $\sigma_{\rm line}$ (and measurement uncertainty) in mean spectra
12	HBETA_FWHM_rms	DOUBLE[2]	km s^{-1}	Hβ FWHM (and measurement uncertainty) in rms spectra
13	HBETA_SIGMA_rms	DOUBLE[2]	km s^{-1}	Hβ $\sigma_{\rm line}$ (and measurement uncertainty) in rms spectra
14	MGII_FWHM_mean	DOUBLE[2]	km s^{-1}	Mg II FWHM (and measurement uncertainty) in mean spectra
15	MGII_SIGMA_mean	DOUBLE[2]	km s^{-1}	Mg II $\sigma_{\rm line}$ (and measurement uncertainty) in mean spectra
16	MGII_FWHM_rms	DOUBLE[2]	km s^{-1}	Mg II FWHM (and measurement uncertainty) in rms spectra
17	MGII_SIGMA_rms	DOUBLE[2]	km s^{-1}	Mg II $\sigma_{\rm line}$ (and measurement uncertainty) in rms spectra
18	R_FE	DOUBLE	⋯	Optical Fe II strength (relative to broad Hβ)
19	REDCHI2_CONTINUUMFIT	DOUBLE[3]	⋯	Reduced χ^2 of the continuum fit around Hα, Hβ, and Mg II
20	REDCHI2_LINEFIT	DOUBLE[3]	⋯	Reduced χ^2 of line fit of Hα, Hβ, and Mg II
21	FLAG_GOOD_MEAN_HALPHA	INT	⋯	value 1 (0) indicates in (not in) the Hα good mean subsample
22	FLAG_GOOD_RMS_HALPHA	INT	⋯	value 1 (0) indicates in (not in) the Hα good rms subsample
23	FLAG_GOOD_MEAN_HBETA	INT	⋯	value 1 (0) indicates in (not in) the Hβ good mean subsample
24	FLAG_GOOD_RMS_HBETA	INT	⋯	value 1 (0) indicates in (not in) the Hβ good rms subsample
25	FLAG_GOOD_MEAN_MGII	INT	⋯	value 1 (0) indicates in (not in) the Mg II good mean subsample
26	FLAG_GOOD_RMS_MGII	INT	⋯	value 1 (0) indicates in (not in) the Mg II good rms subsample

(This table is available in its entirety in FITS format.)

the adjacent narrow-line (or blended line) removal. Appendix B provides a detailed discussion on our window choice.

We employed the Monte Carlo approach described in Shen et al. (2008, 2011) to estimate uncertainties in the line width measurements. To create a mock spectrum, the original spectrum is perturbed at each pixel by a random deviation drawn from a Gaussian distribution whose σ is set to the flux density uncertainty at that pixel. After generating a mock spectrum, we apply the same fitting approach to derive the spectral measurements. We generate 50 mock spectra for each object and estimate the measurement uncertainty as the semi-amplitude of the range enclosing the 16th and 84th percentiles of the distribution.

3.4. Subsamples with Good Quality

In order to mitigate the effects of low-quality measurements, we select subsamples with good quality in their fitting results, which are designated as the "good" samples. For mean spectrum line width measurements, we select a high-S/N subsample using

$$\{\mathrm{S/N}\}_{\rm line,mean} > 3, \tag{5}$$

where $\{\mathrm{S/N}\}_{\rm line,mean}$ is the average flux-to-uncertainty ratio in the total-flux mean spectrum within the line-fitting window.

Two additional criteria are imposed to require that the mean line widths are well measured:

$$\mathrm{FWHM}_{\rm mean}/\mathrm{FWHM}_{\rm mean,error} > 3, \tag{6}$$

$$\sigma_{\rm line,mean}/\sigma_{\rm line,mean,error} > 3. \tag{7}$$

In addition to the above quantitative criteria, we also visually inspected the fits to the mean spectra and excluded objects where the spectrum is heavily affected by skylines, has moderate to strong absorption features, or covers less than half of the profile, or where the model clearly failed to account for the complex profile. In total, 11 Hβ, 6 Hα, and 67 Mg II cases are excluded from our visual inspection.

For rms spectrum line width measurements, we first select a high-variability subsample using

$$\{\mathrm{S/N}\}_{\rm lightcurve} = \sqrt{\chi^2_{\rm lightcurve} - (N_{\rm epoch} - 1)} > 10, \tag{8}$$

where $\{\mathrm{S/N}\}_{\rm lightcurve}$ quantifies the intrinsic variability of the broad-line light curve (equivalent to "SNR2" in the sample catalog compiled by Shen et al. 2019). We set this criterion to ensure that the rms line profile is well determined by PrepSpec and dominated by intrinsic broad emission line variability. As for the mean line widths, the following equations are imposed to require that the rms line widths are well measured:

$$\mathrm{FWHM}_{\rm rms}/\mathrm{FWHM}_{\rm rms,error} > 3, \tag{9}$$

$$\sigma_{\rm line,rms}/\sigma_{\rm line,rms,error} > 3. \tag{10}$$

For comparisons involving only mean line widths, the criteria are Equations (5)–(7), while the criteria are Equations (8)–(10) for comparisons only involving rms line widths. For comparisons involving both mean and rms line widths, all criteria are included. The number of objects that cover each line and the number of objects in the good subsamples that pass the criteria are listed in Table 2. The measured line widths with all four definitions for Hα, Hβ, and Mg II, along with additional fitting parameters, are provided in an online FITS table; its content is summarized in Table 3.

Table 4
Statistics of Mean and rms Line Width Correlations for the Same Line

Line	Line Width Definition	a	b	ϵ_0	r	Sample
Hβ	FWHM	0.05 ± 0.01	0.93 ± 0.04	0.05 ± 0.01	0.91	C06
	$\sigma_{\rm line}$	0.04 ± 0.01	0.58 ± 0.09	0.09 ± 0.01	0.63	C06
Hβ	FWHM	−0.01 ± 0.01	0.76 ± 0.05	0.08 ± 0.01	0.87	SDSS-RM
	$\sigma_{\rm line}$	−0.01 ± 0.01	0.77 ± 0.04	0.05 ± 0.01	0.93	SDSS-RM
Hα	FWHM	−0.03 ± 0.01	0.88 ± 0.07	0.07 ± 0.01	0.91	SDSS-RM
	$\sigma_{\rm line}$	0.01 ± 0.01	0.90 ± 0.06	0.05 ± 0.01	0.94	SDSS-RM
Mg II	FWHM	−0.05 ± 0.01	0.67 ± 0.04	0.09 ± 0.01	0.70	SDSS-RM
	$\sigma_{\rm line}$	−0.04 ± 0.01	0.81 ± 0.02	0.04 ± 0.01	0.93	SDSS-RM

Note. Columns (1) and (2) show the line name and line width definition choice studied in each row, respectively. Columns (3), (4), and (5) give the intercept a, slope b, and intrinsic scatter ϵ_0 (in units of dex) from our Bayesian linear regression fitting between mean and rms line widths (see Section 4.1), respectively. Column (6) gives the Pearson correlation coefficient r. The last column denotes the sample used to derive those parameters.

4. Line Width Comparison

4.1. Mean and rms Widths for the Same Line

In this section we use the good mean and rms subsamples to investigate how the mean and rms line widths correlate for the same line. Apart from SDSS-RM sample, we also include 35 objects from C06 with mean and rms width measurements of Hβ. We use the Pearson correlation test to evaluate the significance of each correlation. The Pearson coefficient r reflects the correlation between two quantities, i.e., a value close to 1 indicates that they are tightly correlated. We list the values of r for both FWHM and $\sigma_{\rm line}$ and for Hβ, Hα, and Mg II in Table 4 and denote them in the upper left corner of each panel in Figure 2. r for the C06 Hβ sample are also listed in Table 4 for comparison. The slopes of these correlations are measured using the Bayesian linear regression method of Kelly (2007). We fit in log–log space using the following equation:

$$\log(W_{\rm mean}/W_0) = a + b\,\log(W_{\rm rms}/W_0) + \epsilon_0, \qquad (11)$$

where a, b, and ϵ_0 are the intercept, slope, and intrinsic scatter, respectively. $W_{\rm mean}$ and $W_{\rm rms}$ refer to FWHM or $\sigma_{\rm line}$ from the mean and rms spectrum. W_0 is the reference point of the regression fit, whose value is set to 4000 km s^{-1} for FWHM and 2000 km s^{-1} for $\sigma_{\rm line}$, respectively, for both mean and rms line widths. The best-fit parameters, their errors, and the intrinsic scatters are listed in Table 4.

Figure 2 compares mean and rms widths for Hβ, Hα, and Mg II in each row, respectively. It shows that in general there are strong correlations between the mean and rms widths for each line. Hα shows slopes close to 1 within 2σ; Hβ shows slopes slightly shallower but is consistent with a linear correlation. The only exception is the correlation between FWHM$_{\rm mean}$ and FWHM$_{\rm rms}$ of Mg II. It shows a mildly larger scatter and a more nonlinear slope than those of the two Balmer lines. This difference is at least partly due to the difficulty of modeling the Mg II line in the presence of strong UV Fe II emission and our neglect of the fact that Mg II is a doublet. The choice of Fe II template may also make a difference (Ho et al. 2012). Nevertheless, the strong correlation between Mg II $\sigma_{\rm line,mean}$ and $\sigma_{\rm line,rms}$ indicates that $\sigma_{\rm line}$ is well correlated between the mean and the variable component of the line; therefore, $\sigma_{\rm line,mean}$ could be a better single-epoch virial velocity estimator than FWHM$_{\rm mean}$ for Mg II.

C06 reported that for Hβ, the rms line widths are typically ∼20% lower than the mean line widths. As demonstrated by Barth et al. (2015), it can be affected by the method of constructing the rms spectrum. The line-only rms spectra generated by Barth et al. (2015) and PrepSpec better represent the variability in the broad lines and should provide more reliable rms line widths; this improvement probably explains why we find little systematic offset between the mean and rms line widths displayed in Figure 2. Nevertheless, consistent with C06, we find a strong correlation between the mean and rms widths for Hβ.

The correlations between the rms widths and the mean widths provide important justification for single-epoch BH mass recipes, where the widths measured from the single-epoch spectrum are used as a surrogate for the virial velocity of the BLR.

4.2. Mean and rms Widths between Different Lines

We now compare the line widths between different broad lines. We adopt Hβ as the reference line in this comparison, since it is the primary line for most RM work in the past and is most commonly used for BH mass estimation. In each comparison we use the same width definition for both lines. The comparisons for the four different width definitions are shown in Figure 3 (Hα vs. Hβ) and Figure 4 (Mg II vs. Hβ). Only objects included in the good subsamples are used in this comparison.

As with our analysis in Section 4.1, we perform the Pearson correlation test and the Bayesian linear regression on the comparisons between different lines, and the results are summarized in Table 5. Consistent with earlier work (e.g., Greene & Ho 2005; Shen et al. 2008, 2011; Shen & Liu 2012; Wang et al. 2009), there are reasonably good correlations between the broad-line widths among the two Balmer lines and Mg II.

Hα and Hβ are strongly correlated, with slopes close to unity and low scatter. This indicates that Hα widths can be used to substitute for Hβ widths, once the slight difference between the two lines is taken into account. We confirmed that the correlation between Mg II and Hβ widths is sublinear using mean line widths (Wang et al. 2009). The correlation between Mg II and Hβ rms line widths is much stronger, suggesting that the variable component of Mg II may also contain information about the virial velocity of the BLR, just as is the case for the Balmer lines.

All previous comparisons between two different lines in earlier work were for the widths measured from the mean

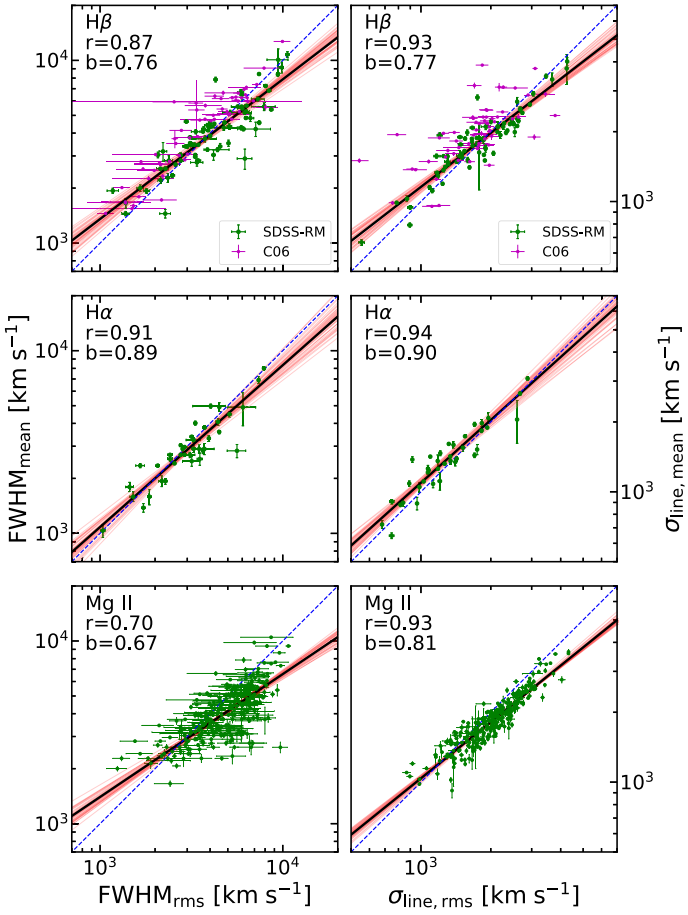

Figure 2. Comparison between FWHM in the mean and rms spectra (left three panels) and $\sigma_{\rm line}$ in the mean and rms spectra (right three panels) for Hβ, Hα, and Mg II from top to bottom, respectively. Green points with error bars are the SDSS-RM sample, while magenta points represent the C06 Hβ-only sample. The blue dashed line in each panel is the 1:1 line. For each comparison, we perform the Bayesian linear regression on the data following Kelly (2007). Black solid lines are the median relations from the Bayesian fit, and the red shaded regions are the 1σ confidence ranges of the fit. The Pearson correlation coefficient r and the best-fit slope b from the linear regression are shown in the upper left corner in each panel.

spectra, and our study here presents the first systematic cross-line comparison for the widths measured from the rms spectra. The correlations between the widths for different lines provide the justification for using Hα or Mg II as an alternative to Hβ for virial BH mass estimation.

5. Discussion

5.1. Which Line Width Is a Better Virial Velocity Indicator?

To evaluate which line width best indicates the BLR virial velocity and therefore produces the most reliable BH mass estimation, we perform the same test in Collin et al. (2006). We assume that the BH masses independently estimated from the $M_{\rm BH}$–σ_* relation, $M_{{\rm BH},\sigma_*}$, are reliable and unbiased, and we use them as the reference (but see caveats discussed later in Section 5.1). The virial coefficient f can be computed via the following equation:

$$M_{{\rm BH},\sigma_*} = f \times \frac{W^2\,(c\,\tau)}{G}, \tag{12}$$

where W is the broad-line velocity width, either FWHM or $\sigma_{\rm line}$; $c\tau$ reflects the average distance of the BLR from the BH; and G is the gravitational constant.

Under the assumption that active and inactive galaxies share the same $M_{\rm BH}$–σ_* relation, Onken et al. (2004) used 14 RM AGNs with host σ_* measurements and obtained an average virial coefficient $\langle f\rangle = 5.5 \pm 1.8$ using $\sigma_{\rm line,rms}$. Woo et al. (2010, 2013) obtained $\langle f\rangle = 5.1^{+1.5}_{-1.1}$ if using only active galaxies, and Grier et al. (2013) obtained $\langle f\rangle = 4.31 \pm 1.05$; both were consistent with Onken et al. (2004). However, Graham et al. (2011) obtained a virial coefficient of $\langle f\rangle = 2.8^{+0.7}_{-0.5}$, which is only half of those reported in previous work.

In order to address the question of which line width definition is a better indicator for the virial velocity, we compare the virial products (VPs) based on each line width definition with the host stellar velocity dispersion and investigate which line width produces the lowest scatter and least variance in f among different subsets of the sample. We adopt Hβ for this study throughout this section since most objects with σ_* measurements have only Hβ coverage.

Ho & Kim (2014, hereafter HK14) compiled all available local RM AGNs with σ_* measurements and further divided them into subsets of classical bulges (CBs) and pseudobulges (PBs). Their study consisted of 35 objects with all four line width definitions, lags, and σ_* measurements available from the literature (see Table 2 in HK14). In SDSS-RM, there are

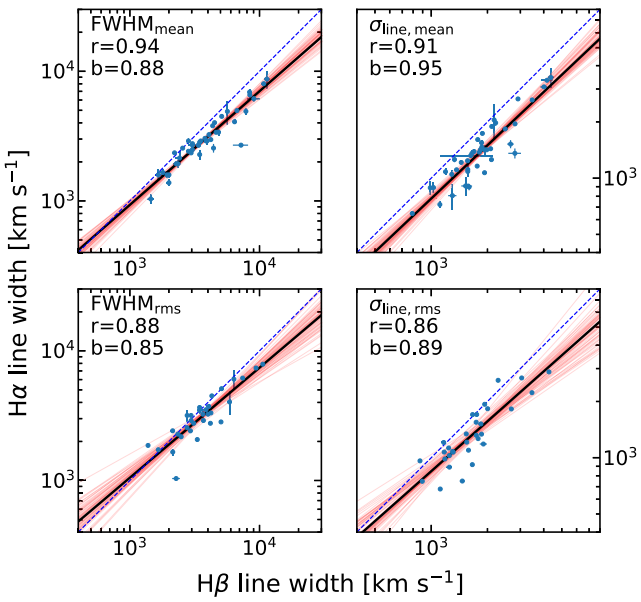

Figure 3. Comparison of the line widths between Hα and Hβ using four different line width definitions. Blue points with error bars in the top two panels are objects selected from the good mean Hβ and good mean Hα subsamples. Blue points with error bars in the bottom two panels represent objects selected from the good rms Hβ and good rms Hα subsamples. Blue dashed lines are the 1:1 correlation. For each line width definition, we perform the Bayesian linear regression fit on the data. Black solid lines are the median relation from the Bayesian fit, and the red shaded regions are the 1σ confidence range of the fit. The Pearson correlation coefficients r and slopes b are shown in the upper left corner of each panel.

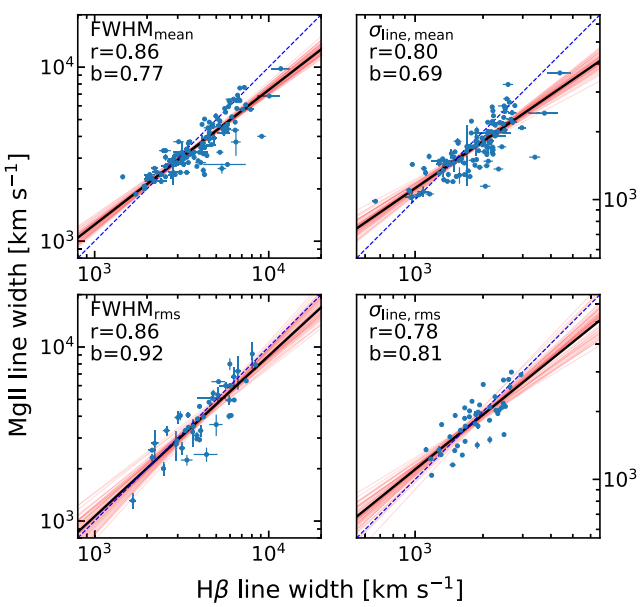

Figure 4. Same format as Figure 3, but for comparison of Mg II and Hβ. Blue points with error bars in the top two panels represent objects selected from the good mean Hβ and good mean Mg II subsample. Blue points with error bars in the bottom two panels represent objects selected as the good rms Hβ and good rms Mg II subsample.

currently 20 objects with all measurements available from the first-year data. For these objects, their σ_* measurements are taken from Shen et al. (2015b), where successful σ_* measurements meet the criteria that they are measured at $>3\sigma$ confidence level, their σ_* error warning flag is set to zero, and their host galaxy fraction is larger than 0.05. Their Hβ lag measurements are taken from Grier et al. (2017), where successful lag measurements mean that they are at $>2\sigma$ significance. We cross-match them with our good mean and rms subsample and obtain our final sample. Combined with the HK14 objects, our joint sample includes 55 objects with all quantities available.

Following HK14, we express the relation between VP and σ_* for our quasar sample as

$$\log\left(\frac{\mathrm{VP}}{M_\odot}\right) = \alpha - \log f + \beta \log\left(\frac{\sigma_*}{200\ \mathrm{km\ s^{-1}}}\right), \quad (13)$$

where α is the normalization, β is the slope of the M–σ_* relation, and $\mathrm{VP} \equiv W^2 c\tau/G$ is the virial product from RM observations. We use Markov chain Monte Carlo to perform a linear regression to minimize the quantity:

$$\chi^2 = \sum_{i=1}^{N} \frac{(y_i + \log f - \alpha - \beta x_i)^2}{\epsilon_{yi}^2 + \beta^2 \epsilon_{xi}^2 + \epsilon_0^2}. \quad (14)$$

In the regression fit we fix $\alpha = 8.49$ and $\beta = 4.38$, from the M_{BH}–σ_* relation for hosts classified as CBs in Kormendy & Ho (2013, see their Equation (7)).[13] The results are presented in Figure 5 for the four line width definitions. The intrinsic scatter ϵ_0 is shown in the upper left corner of each panel and in Table 6. While the result based on $\sigma_{\mathrm{line,mean}}$ has the lowest scatter, the scatter is mutually consistent among the results using all four line width definitions, indicating that our current sample size is insufficient to conclude which width definition is best for virial BH mass estimation based on this particular test.

Table 6 also summarizes our estimates of the average virial coefficient $\langle f \rangle$ based on different width definitions of Hβ for the full sample of 55 objects. Our best-fit virial coefficients $\langle f \rangle$ using $\sigma_{\mathrm{line,rms}}$ are 6.23 ± 1.15, which are fully consistent within error bars with those reported in Onken et al. (2004), Woo et al. (2013), and Grier et al. (2013).

Another test to evaluate the line width choice is to investigate whether the virial coefficient is consistent among different subpopulations of quasars. Following C06, we divide our joint sample into four subpopulations, Population 1/Population 2 and Population A/Population B. Population 1 and Population 2 are divided using

$$\mathrm{FWHM_{mean}}/\sigma_{\mathrm{line,mean}} \sim 2, \quad (15)$$

with Population 1 having smaller ratios. We also divide the sample into Population A and Population B according to

$$\mathrm{FWHM_{mean}} \sim 4000\ \mathrm{km\ s^{-1}}, \quad (16)$$

with Population A having smaller $\mathrm{FWHM_{mean}}$. The two criteria are slightly different from those of C06, who used $\mathrm{FWHM_{mean}}/\sigma_{\mathrm{line,mean}} \sim 2.35$ (value of a Gaussian profile) and $\sigma_{\mathrm{line,mean}} \sim 2000\ \mathrm{km\ s^{-1}}$. However, to make the subsamples comparable in size between Population 1 and Population 2, we choose the division at $\mathrm{FWHM_{mean}}/\sigma_{\mathrm{line,mean}} \sim 2$. The other criterion in C06 is equivalent to ours because the mean ratio of $\mathrm{FWHM_{mean}}/\sigma_{\mathrm{line,mean}}$ is around 2. With our sample division, there are 26 (29) Population 1 (Population 2) objects and 31 (24) Population A (Population B) objects.

[13] Since we lack bulge type information for the SDSS-RM sample, we cannot divide the sample into CBs and PBs as done in HK14. We treat all objects in our sample as CBs.

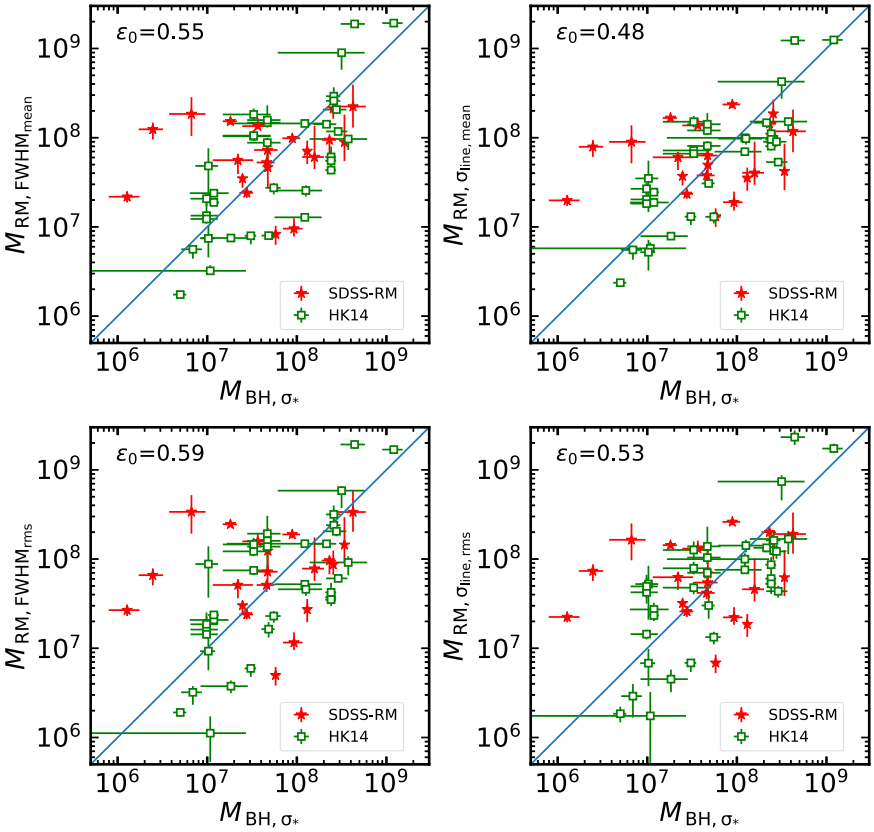

Figure 5. Comparison between RM masses derived by multiplying the virial products with an averaged virial coefficient and masses from the $M_{\rm BH}$–σ_* relation. The four panels are results using four different line width definitions. The intrinsic scatter is labeled in the upper left corner of each panel. Red stars denote SDSS-RM objects, and green open squares are the HK14 sample. Blue solid lines represent the 1:1 correlation.

Table 5
Statistics of Line Width Comparison between Different Lines

	Line Width Definition	a	b	ϵ_0	r
Hα versus Hβ	FWHM$_{\rm mean}$	-0.10 ± 0.01	0.88 ± 0.05	0.05 ± 0.01	0.94
	$\sigma_{\rm line,mean}$	-0.12 ± 0.01	0.95 ± 0.07	0.07 ± 0.01	0.91
	FWHM$_{\rm rms}$	-0.07 ± 0.02	0.84 ± 0.10	0.10 ± 0.01	0.88
	$\sigma_{\rm line,rms}$	-0.11 ± 0.02	0.89 ± 0.09	0.09 ± 0.01	0.86
Mg II versus Hβ	FWHM$_{\rm mean}$	-0.04 ± 0.01	0.77 ± 0.04	0.07 ± 0.01	0.86
	$\sigma_{\rm line,mean}$	-0.04 ± 0.01	0.69 ± 0.05	0.07 ± 0.01	0.80
	FWHM$_{\rm rms}$	-0.02 ± 0.01	0.92 ± 0.09	0.09 ± 0.01	0.86
	$\sigma_{\rm line,rms}$	-0.01 ± 0.01	0.81 ± 0.11	0.07 ± 0.01	0.78

Note. We use the same notation as in Table 4.

In addition to using line width to divide the sample, we also use the Hβ line-continuum flux ratio, $f(\mathrm{H}\beta)/f_\lambda(5100)$, as a proxy for H$\beta$ line strength (direct measurements of Hβ equivalent width are not publicly available for the HK14 sample) to divide the joint sample into Population C/Population D. The division is

$$f(\mathrm{H}\beta)/f_\lambda(5100) \sim 60\ [\text{Å}], \tag{17}$$

with Population C having smaller ratios. There are 26 objects in Population C and 28 objects in Population D.

Table 7 lists the average virial coefficients $\langle f \rangle$ of different subpopulations for the four line width definitions. For both FWHM$_{\rm mean}$ and FWHM$_{\rm rms}$, there is a large difference in the virial coefficient between Population 1/Population 2 and between Population A/Population B. On the other hand, for both $\sigma_{\rm line,mean}$ and $\sigma_{\rm line,rms}$, the virial coefficients are more consistent across the four different subpopulations. The $\sigma_{\rm line,mean}$ provides the most consistent virial coefficient among these four different quasar subpopulations. These findings are consistent with C06. One interpretation is that FWHM is likely affected by additional parameters that do not trace the underlying virial velocity, such as the orientation of a flattened BLR (e.g., Wills & Browne 1986; Collin et al. 2006; Shen & Ho 2014; Brotherton et al. 2015;

Table 6
Virial Coefficient f and Intrinsic Scatter ϵ_0 in the VP–σ_* Correlation

Width Definition	f	ϵ_0
$\mathrm{FWHM_{mean}}$	1.19 ± 0.22	0.55 ± 0.06
$\sigma_{\mathrm{line,mean}}$	4.63 ± 0.75	0.48 ± 0.06
$\mathrm{FWHM_{rms}}$	1.53 ± 0.30	0.59 ± 0.07
$\sigma_{\mathrm{line,rms}}$	6.23 ± 1.15	0.54 ± 0.06

Table 7
Virial Coefficients for Different Subpopulations

	$\mathrm{FWHM_{mean}}$	$\sigma_{\mathrm{line,mean}}$	$\mathrm{FWHM_{rms}}$	$\sigma_{\mathrm{line,rms}}$
Population 1	2.21 ± 0.56	5.33 ± 1.09	2.74 ± 0.76	8.05 ± 2.01
Population 2	0.68 ± 0.16	4.24 ± 1.13	0.95 ± 0.25	5.18 ± 1.46
Population A	1.81 ± 0.44	4.86 ± 0.97	2.21 ± 0.59	6.99 ± 1.64
Population B	0.72 ± 0.19	4.63 ± 1.38	1.01 ± 0.31	5.77 ± 1.82
Population C	1.44 ± 0.43	5.72 ± 1.54	1.97 ± 0.63	8.29 ± 2.44
Population D	1.03 ± 0.27	3.73 ± 0.77	1.23 ± 0.32	4.72 ± 1.10
All	1.19 ± 0.22	4.63 ± 0.75	1.53 ± 0.30	6.21 ± 1.13
HK14 CB	1.5 ± 0.4	6.3 ± 1.5	1.3 ± 0.4	5.6 ± 1.3
HK14 PB	0.7±0.2	3.2 ± 0.7	0.5 ± 0.2	1.9 ± 0.7

Note. Columns (2)–(5) list the virial coefficients based on each line width definition. Rows 1–6 are virial coefficients calculated using different subpopulations, and row 7 is for the full joint sample. The values in rows 8 and 9 are virial coefficients of subsamples with CB and PB taken from Table 3 in HK14.

Mejía-Restrepo et al. 2018), whereas σ_{line} is less sensitive to such parameters.

On the other hand, we find that for both $\mathrm{FWHM_{mean}}$ and $\mathrm{FWHM_{rms}}$ the virial coefficients are consistent across Population C/Population D, while for both $\sigma_{\mathrm{line,mean}}$ and $\sigma_{\mathrm{line,rms}}$ there is a slightly larger difference (only marginally significant) across Population C/Population D. Our previous test comparing the correlations between VPs and host σ_* also revealed that using σ_{line} produces just as much scatter as using FWHM (e.g., Figure 5). This could mean that additional factors (other than orientation) likely degrade the correlation between σ_{line} and the underlying virial velocity, or even introduce some bias in using σ_{line}. One possibility is that σ_{line} could be measuring parts of the velocities that do not tightly correspond to the virial velocity (e.g., outflows or kinematic components in the profile wings that do not reverberate to the ionizing continuum). Alternatively, σ_{line} could indeed be a more reliable indicator for the virial velocity, but this fact is clouded by the systematic uncertainties in the measured quantities that led to Figure 5, the intrinsic scatter in the M_{BH}–σ_* relation, the limited sample size, etc. For example, some σ_* measurements may be contaminated by a rotational disk and suffer from orientation effects to some degree, which will introduce extra scatter in the correlation tests in Figure 5. A larger RM sample with more host bulge σ_* measurements is needed to further test these scenarios.

5.2. Broad-line Shapes

Since FWHM is more sensitive to the core of the line while σ_{line} depends more on the wings, the ratio $\mathrm{FWHM}/\sigma_{\mathrm{line}}$ can be used as a line shape parameter to characterize the line profile. A Gaussian profile has an $\mathrm{FWHM}/\sigma_{\mathrm{line}}$ ratio of 2.35; values larger (smaller) than this indicate a higher (lower) fraction of flux in the core than in the wings relative to that for a Gaussian.

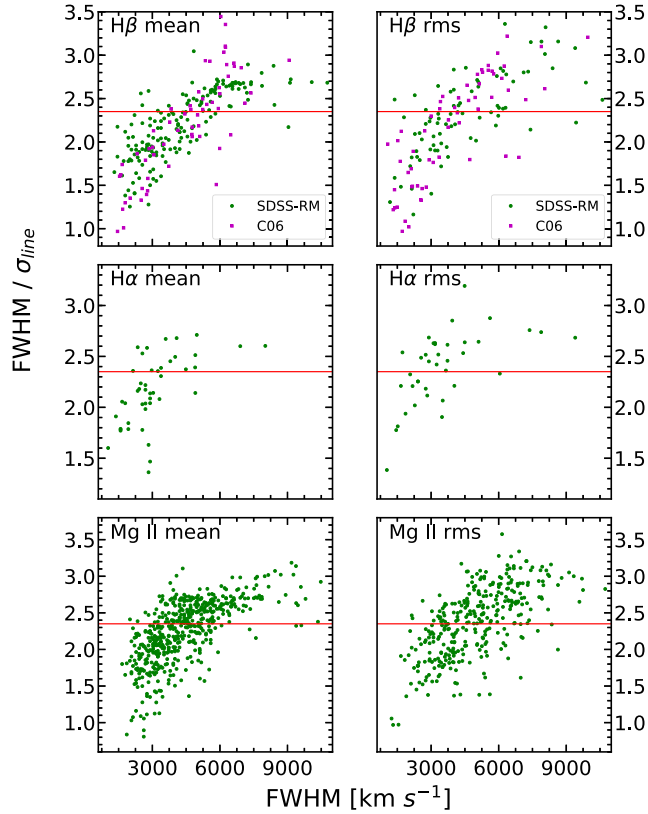

Figure 6. Line shape parameter $\mathrm{FWHM}/\sigma_{\mathrm{line}}$ as a function of FWHM of mean spectra (left) and rms spectra (right). The results for Hβ, Hα, and Mg II are shown from top to bottom, respectively. The red horizontal line corresponds to the Gaussian profile with $\mathrm{FWHM}/\sigma_{\mathrm{line}} = 2.35$.

Table 8
Pearson Correlation Coefficients r between the Ratio $\mathrm{FWHM}/\sigma_{\mathrm{line}}$ and FWHM

	Hβ	Hα	Mg II
Mean spectra	0.75	0.59	0.65
rms spectra	0.69	0.50	0.63

Figure 6 demonstrates that the line shape parameter changes as a function of FWHM in mean and rms spectra. There is a trend that the profile becomes more centrally concentrated when FWHM increases. The Pearson correlation coefficients of the trends are presented in Table 8. This trend is obvious for both mean and rms profiles and for all three lines. The fact that this trend is not linear (as expected from pure self-correlation owing to the common FWHM in both quantities) indicates that σ_{line} varies in the same direction as FWHM, but with a lower amplitude.

We further investigate the line profile changing along the Eigenvector 1 (EV1) sequence of quasars. EV1 is a physical sequence that correlates most of the observed quasar properties with the strength of the optical Fe II emission (e.g., Boroson & Green 1992; Sulentic et al. 2000; Shen & Ho 2014). In the 2D plane of broad Hβ FWHM versus $R_{\mathrm{Fe\,II}} \equiv \mathrm{EW_{Fe\,II,4434-4684}}/\mathrm{EW_{H\beta}}$, EV1 is defined as a band extending from low to high $R_{\mathrm{Fe\,II}}$ with decreasing average broad Hβ FWHM. Shen & Ho (2014) suggested that the vertical dispersion in broad Hβ FWHM in the EV1 plane is mainly due to an orientation effect (combined with any intrinsic dispersion of line width due to different BH masses

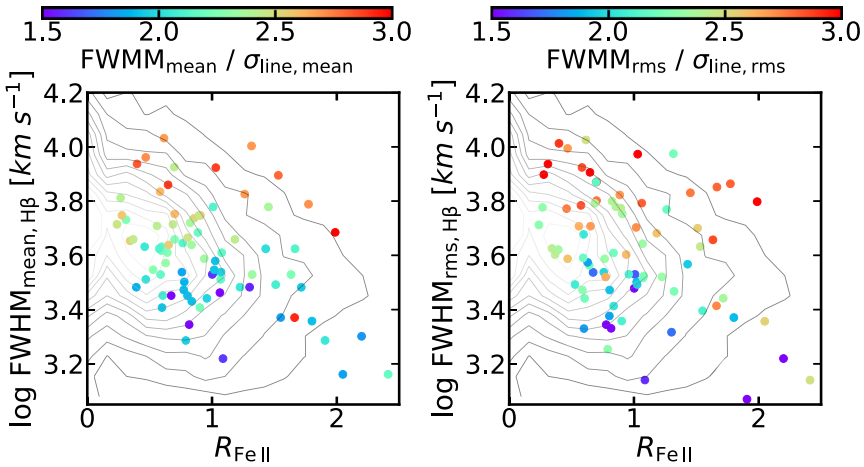

Figure 7. Distribution of the SDSS-RM sample in the EV1 plane color-coded by the line shape parameter FWHM/σ_{line}, for the mean widths (left) and rms widths (right). In both panels there is a clear segregation of colors that tracks the EV1 sequence. The distributions of the SDSS DR7 quasars from Shen et al. (2011) are indicated as the gray contours.

sampled), where the differences in FWHM reflect the changes in the orientation of a flattened BLR along the line of sight. If this interpretation is correct, there should be a similar vertical dispersion of the shape parameter within the EV1 sequence, if σ_{line} is less susceptible to orientation.

Figure 7 shows the distribution of the broad Hβ shape parameter in the EV1 plane. We use FWHM and σ_{line} from either mean or rms spectra and compute the shape parameter from their ratios. The shape parameter measured from the mean spectrum (left panel) displays a clear vertical segregation at fixed $R_{Fe\,II}$, consistent with the findings in Shen & Ho (2014, see their Figure E10). A similar trend exists for the shape parameter measured from the rms spectrum (right panel of Figure 7). Interestingly, the segregation of objects with different line shapes more or less tracks the main EV1 sequence such that the running median of the distribution at fixed $R_{Fe\,II}$ has roughly the same line shape parameter. This result is fully consistent with the framework discussed in Shen & Ho (2014), where the running median of the EV1 sequence represents the average orientation of a flattened BLR, and vertical deviations from the median correspond to variations of the orientation and hence the changes in the line shape parameter.

6. Conclusions

We have investigated different definitions of line widths from the mean and rms spectra for three low-ionization broad lines, Hα, Hβ, and Mg II, using the sample of quasars from the SDSS-RM project. For each of the three lines, we fit and measured the broad-line FWHM and σ_{line} from the mean and rms spectra derived from the first-season spectroscopic observations of SDSS-RM. We compared different definitions of line widths for the same line and compared the same line widths among different lines.

The main results from this study are as follows:

1. We introduced a new recipe to measure σ_{line} that is reproducible, is less susceptible to noise and blending in the wings, and scales with the intrinsic width of the line. This quantitative recipe can be used to measure consistent σ_{line} values by different groups.
2. There are significant correlations between different line widths for the same line. Since most of the RM BH masses to date are based on the rms σ_{line}, the correlations between other width definitions and σ_{line} provide justification for using the other width definitions for single-epoch virial BH mass estimation where only the mean FWHM and σ_{line} are available.
3. There are also strong correlations between the line widths for different lines. The consistency in broad-line widths between the other two lines (Hα and Mg II) and the Hβ line provides the justification for using these alternative lines rather than Hβ to estimate virial BH masses.
4. We investigated the correlations between the RM virial products based on different width definitions and the host stellar velocity dispersion σ_*, using a sample of 55 quasars with both RM and σ_* measurements. We calculated the virial coefficient f using the σ_* measurements for different width definitions and for different subpopulations of quasars. Consistent with C06, we found that the virial coefficient using σ_{line} is more or less consistent across subpopulations divided by line width, while the virial coefficient using FWHM has a large dispersion among these subpopulations. On the other hand, the virial coefficient using σ_{line} is less consistent than that using FWHM across subpopulations divided by line strength, although the significance of the difference is low. The correlation analysis for the virial product versus stellar velocity dispersion for the full sample does not provide conclusive evidence that any of the line width definitions are better than the others.
5. We studied the shape of the broad Hβ line, characterized by FWHM/σ_{line}, as functions of quasar parameters. Consistent with Shen & Ho (2014), we found that the shape parameter displays a segregation in the EV1 plane that closely follows the sequence along EV1, which again suggests that orientation plays a stronger role in changing the FWHM of the line than σ_{line}.

Our results are consistent with earlier studies (e.g., Greene & Ho 2005; Collin et al. 2006; Shen et al. 2008, 2011; Wang et al. 2009; Shen & Liu 2012) but extend to all four line width definitions with a much larger RM sample and for all three low-ionization broad lines. In particular, the comparisons involving the rms widths of Hα and Mg II are presented here for the first time.

Although our results corroborate earlier suggestions that FWHM may be more impacted by orientation effects in a flattened BLR than $\sigma_{\rm line}$ (e.g., Wills & Browne 1986; Runnoe et al. 2013; Shen & Ho 2014; Brotherton et al. 2015; Mejía-Restrepo et al. 2018), it does not necessarily mean that $\sigma_{\rm line}$ is a more accurate tracer of the virial velocity for the broad lines. $\sigma_{\rm line}$ is sensitive to the wings of the line, which may not reverberate to continuum changes and/or may arise in a nonvirial component. To determine whether FWHM or $\sigma_{\rm line}$ is a better tracer of the virial velocity, additional data are required for two case studies: (1) a large sample of quasars with both host stellar velocity dispersion and broad-line width measurements to determine which width definition produces the tightest correlation between the virial product and the stellar velocity dispersion, and (2) a large sample of quasars with large dynamical range in their continuum variability to test which width definition best follows the expected virial relation (e.g., Peterson et al. 2004; Shen 2013). Our attempt on this first case study did not yield conclusive results, but future larger samples with both RM and σ_* measurements may clarify the situation. The SDSS-RM project will compile multiyear light curves for 849 quasars and thus will provide one of the best samples for the second investigation. In addition, the multiyear data from SDSS-RM will be used to extend our line width study to other broad lines (such as C IV) covered in the high-redshift subsample.

We thank Brad Peterson and the anonymous referee for suggestions that improved this work. We acknowledge support from the National Key R&D Program of China (2016YFA0400703), the National Science Foundation of China (11533001, 11721303, 11890693), and the Chinese Academy of Sciences (CAS) through a China-Chile Joint Research Fund No. 1503 administered by the CAS South America Center for Astronomy. Y.S. acknowledges support from an Alfred P. Sloan Research Fellowship and NSF grant AST-1715579. K.H. acknowledges support from STFC grant ST/R000824/1. C.J.G. acknowledges support from NSF grant AST-1517113. W.N.B. acknowledges support from NSF grants AST-1517113 and AST-1516784.

Funding for SDSS-III has been provided by the Alfred P. Sloan Foundation, the Participating Institutions, the National Science Foundation, and the U.S. Department of Energy Office of Science. The SDSS-III website is http://www.sdss3.org/.

SDSS-III is managed by the Astrophysical Research Consortium for the Participating Institutions of the SDSS-III Collaboration, including the University of Arizona, the Brazilian Participation Group, Brookhaven National Laboratory, University of Cambridge, Carnegie Mellon University, University of Florida, the French Participation Group, the German Participation Group, Harvard University, the Instituto de Astrofisica de Canarias, the Michigan State/Notre Dame/JINA Participation Group, Johns Hopkins University, Lawrence Berkeley National Laboratory, Max Planck Institute for Astrophysics, Max Planck Institute for Extraterrestrial Physics, New Mexico State University, New York University, Ohio State University, Pennsylvania State University, University of Portsmouth, Princeton University, the Spanish Participation Group, University of Tokyo, University of Utah, Vanderbilt University, University of Virginia, University of Washington, and Yale University.

Appendix A
Simulations of the rms Spectrum Generation

As mentioned in Section 2, the traditional approach of rms spectrum construction includes the variations from the continuum. Barth et al. (2015) reported that the continuum variation and random noise in the spectrum can cause the generated rms line profile to deviate substantially from the true rms line profile, that is, solely due to line variation. They adopted a decomposition approach to isolate the continuum component in individual epochs before the construction of the line-only rms spectrum, similar to our PrepSpec approach. They used simulations to demonstrate the differences in the line rms profile from these two approaches, and below we perform a similar exercise to reproduce their results.

The numerical experiment is to examine a potential bias in rms line width that occurs when the rms spectrum is constructed from the entire spectrum from individual epochs. To examine this potential bias, we perform a simple simulation to illustrate the difference in the line profile between the two approaches of rms spectrum generation. Using the method of Timmer & Koenig (1995), we construct a random light curve with a certain duration, sampling, power spectrum slope, and rms variability amplitude $F_{\rm var}$. We assume a fluctuation power spectrum $P(\mu) \sim \mu^{-2.7}$, where μ is the frequency in Fourier space. The power-law index is similar to the variability properties of nearby AGNs monitored by the *Kepler* emission (Mushotzky et al. 2011). A series of single-Gaussian line profiles whose line luminosity and width vary in response to continuum fluctuations is generated. For simplification we assume that the integrated luminosity of the line at time t scales linearly with the input continuum light-curve luminosity at time $t - \tau$, where τ is the assumed time lag for the velocity-integrated transfer function. The width of the Gaussian profile also varies accordingly such that the product $\sigma^2 L^{0.5}$ remains constant when luminosity varies, as expected from a perfect virial relation for the line. The broad emission line is set to have a mean equivalent width of 120 Å. The initial width is set to be $\sigma_{\rm line} = 2000\ {\rm km\ s^{-1}}$, and the shape of the continuum is set to be flat over the wavelength range of interest. Spectra are constructed in velocity bins of $60\ {\rm km\ s^{-1}}$. Then, the two sets of spectra, one with emission line only and the other with the total flux including both line and continuum, are created. The FWHM and $\sigma_{\rm line}$ are measured on both sets of rms spectra. Since the continuum and emission-line variations are occasionally out of phase, there could be a pair of local minima in total-flux rms spectrum; in such cases we calculate the σ between the two local minima.

The results of the simulations demonstrate that the total-flux rms spectrum line width could differ significantly from that of the line-only rms spectrum. Figure 8 presents an example of our simulations. In this example, FWHM(total-flux)/FWHM (line-only) is 0.766 and σ(total-flux)/σ(line-only) is 0.740, indicating that the widths measured from the rms spectrum generated by the traditional approach are biased low by ∼20%–30% relative to those measured from the true line rms spectrum.

To quantify the magnitude of this bias, 1000 sets of simulated light curves and spectra with different monitoring durations of 30, 50, and 100 days, assuming nightly sampling, were created. The variability amplitude $F_{\rm var}$ of the continuum light curve is 0.1. Figure 8 shows the bias distribution for both FWHM (bottom left) and $\sigma_{\rm line}$ (bottom right). For both $\sigma_{\rm line}$ and

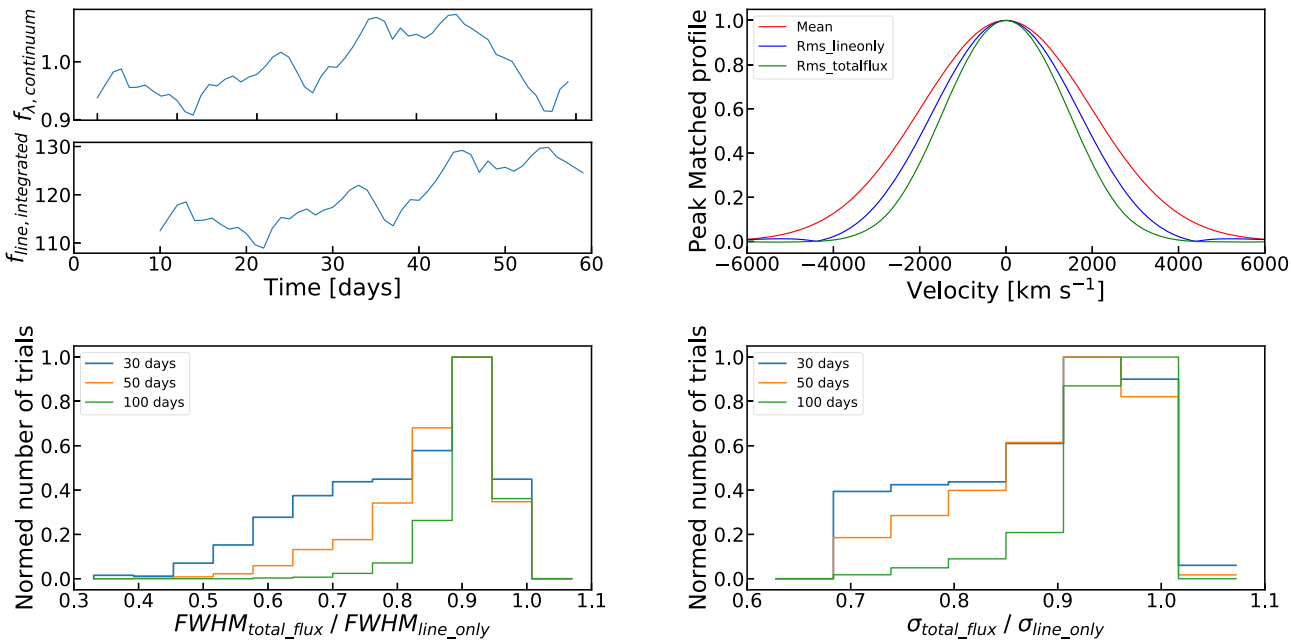

Figure 8. Top left panel: example of simulated continuum and emission-line light curves. The emission-line light curve has a 10-day lag with respect to the continuum light curve. Top right panel: mean spectrum (red), line-only rms spectrum (blue), and total-flux rms spectrum subtracted by a local continuum (green). Bottom panels: distribution of the line width ratios between line width in total_flux rms spectra and line_only rms spectra using FWHM (left) and $\sigma_{\rm line}$ (right), based on 1000 trials for this particular example. The blue, orange, and green histograms refer to 30, 50, and 100 days of the nightly RM observation baseline. Shorter programs can lead to more significantly biased rms line width.

FWHM, the bias in the rms line widths measured from the traditional approach depends on the monitoring duration. For relatively short reverberation mapping programs, the traditional approach can lead to significantly biased rms line width.

Appendix B
The Impact of Windows on the $\sigma_{\rm line}$ Calculation

In the $\sigma_{\rm line}$ calculation the integral kernel is proportional to λ^2; hence, $\sigma_{\rm line}$ is extremely sensitive to the computation window. This behavior is especially true for objects with moderate S/N, where it is difficult to determine the boundaries of the line.

In this work we defined a quantitative window to compute $\sigma_{\rm line}$. This window is determined from the line width measured in the mean spectrum, which typically has much higher S/N than the rms spectrum. We experimented with three choices to define this window, with the half-window size equal to $\rm FWHM_{mean}$, $1.5 \times \rm FWHM_{mean}$, and $2.5 \times \rm MAD_{mean}$ as shown in Figure 9. For mean spectra, the center of the window is chosen as the zero velocity measured from the rest-frame vacuum wavelength, whereas for rms spectra, the center of the window is chosen to be the peak of the rms profile to better include much of the rms flux, since the rms profile is often highly asymmetric. In this example the peak of rms profile is close to the vacuum wavelength, and thus the mean and rms windows are similar.

Based on visual inspection of our objects, the $2.5 \times \rm MAD_{mean}$ half-window size best balances the need to enclose most of the line flux and to avoid noisy wings in the calculation of $\sigma_{\rm line}$. Since this window size scales with the width of the line (e.g., broader lines will yield larger widow sizes), the $\sigma_{\rm line}$ will not be biased as a function of line width, compared to the case

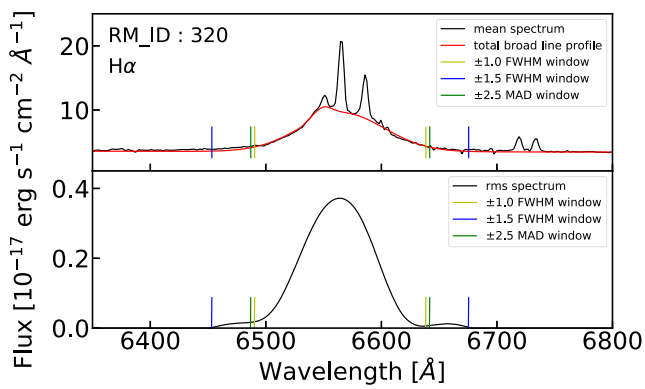

Figure 9. Illustration of the three different choices of window size. The black solid lines in the top and bottom panels represent the mean and rms spectra, respectively. The red line is the total broad-line profile in the mean spectrum used to calculate different line widths. The yellow, blue, and green vertical lines represent $1.0 \times$ FWHM window, $1.5 \times$ FWHM window, and $2.5 \times$ MAD window, respectively.

of a fixed window size. Conversely, the other two window sizes are based on $\rm FWHM_{mean}$, which is sensitive to the central part of the profile. Hence, it is not as good as using $\rm MAD_{mean}$, which includes contributions from the wings. Indeed, the tightest correlations are those with $\sigma_{\rm line}$ calculated using our fiducial window defined by $\rm MAD_{mean}$, compared with those calculated using the windows defined by $\rm FWHM_{mean}$. We therefore adopt $2.5 \times \rm MAD_{mean}$ as the fiducial window to compute $\sigma_{\rm line}$ for both the mean and rms spectra. Each line has its own MAD measurement, and thus different lines in the same object have slightly different window sizes.

ORCID iDs

Shu Wang https://orcid.org/0000-0002-2052-6400
Yue Shen https://orcid.org/0000-0003-1659-7035
Linhua Jiang https://orcid.org/0000-0003-4176-6486
Keith Horne https://orcid.org/0000-0003-1728-0304
W. N. Brandt https://orcid.org/0000-0002-0167-2453
C. J. Grier https://orcid.org/0000-0001-9920-6057
Luis C. Ho https://orcid.org/0000-0001-6947-5846
Yasaman Homayouni https://orcid.org/0000-0002-0957-7151
Jennifer I-Hsiu Li https://orcid.org/0000-0002-0311-2812
Jonathan R. Trump https://orcid.org/0000-0002-1410-0470

References

Alam, S., Albareti, F. D., Allende Prieto, C., et al. 2015, ApJS, 219, 12
Barth, A. J., Bennert, V. N., Canalizo, G., et al. 2015, ApJS, 217, 26
Bentz, M. C., Denney, K. D., Grier, C. J., et al. 2013, ApJ, 767, 149
Blandford, R. D., & McKee, C. F. 1982, ApJ, 255, 419
Boroson, T. A., & Green, R. F. 1992, ApJS, 80, 109
Brotherton, M. S., Singh, V., & Runnoe, J. 2015, MNRAS, 454, 3864
Collin, S., Kawaguchi, T., Peterson, B. M., & Vestergaard, M. 2006, A&A, 456, 75
Eisenstein, D. J., Weinberg, D. H., Agol, E., et al. 2011, AJ, 142, 72
Graham, A. W., Onken, C. A., Athanassoula, E., & Combes, F. 2011, MNRAS, 412, 2211
Greene, J. E., & Ho, L. C. 2005, ApJ, 630, 122
Grier, C. J., Martini, P., Watson, L. C., et al. 2013, ApJ, 773, 90
Grier, C. J., Trump, J. R., Shen, Y., et al. 2017, ApJ, 851, 21
Gunn, J. E., Siegmund, W. A., Mannery, E. J., et al. 2006, AJ, 131, 2332
Ho, L. C., Goldoni, P., Dong, X.-B., Greene, J. E., & Ponti, G. 2012, ApJ, 754, 11
Ho, L. C., & Kim, M. 2014, ApJ, 789, 17
Kaspi, S., Smith, P. S., Netzer, H., et al. 2000, ApJ, 533, 631
Kelly, B. C. 2007, ApJ, 665, 1489
Kormendy, J., & Ho, L. C. 2013, ARA&A, 51, 511
Mejía-Restrepo, J. E., Lira, P., Netzer, H., Trakhtenbrot, B., & Capellupo, D. M. 2018, NatAs, 2, 63
Mushotzky, R. F., Edelson, R., Baumgartner, W., & Gandhi, P. 2011, ApJL, 743, L12
Onken, C. A., Ferrarese, L., Merritt, D., et al. 2004, ApJ, 615, 645
Peterson, B. M. 1993, PASP, 105, 247
Peterson, B. M. 2011, in Narrow-Line Seyfert 1 Galaxies and their Place in the Universe, ed. L. Foschini et al. (Trieste: PoS), 32
Peterson, B. M., Ferrarese, L., Gilbert, K. M., et al. 2004, ApJ, 613, 682
Peterson, B. M., Foltz, C. B., & Byard, P. L. 1981, ApJ, 251, 4
Runnoe, J. C., Brotherton, M. S., Shang, Z., Wills, B. J., & DiPompeo, M. A. 2013, MNRAS, 429, 135
Shen, Y. 2013, BASI, 41, 61
Shen, Y., Brandt, W. N., Dawson, K. S., et al. 2015a, ApJS, 216, 4
Shen, Y., Greene, J. E., Ho, L. C., et al. 2015b, ApJ, 805, 96
Shen, Y., Greene, J. E., Strauss, M. A., Richards, G. T., & Schneider, D. P. 2008, ApJ, 680, 169
Shen, Y., Hall, P. B., Horne, K., et al. 2019, ApJS, 241, 34
Shen, Y., & Ho, L. C. 2014, Natur, 513, 210
Shen, Y., Horne, K., Grier, C. J., et al. 2016, ApJ, 818, 30
Shen, Y., & Liu, X. 2012, ApJ, 753, 125
Shen, Y., Richards, G. T., Strauss, M. A., et al. 2011, ApJS, 194, 45
Smee, S. A., Gunn, J. E., Uomoto, A., et al. 2013, AJ, 146, 32
Sulentic, J. W., Zwitter, T., Marziani, P., & Dultzin-Hacyan, D. 2000, ApJL, 536, L5
Timmer, J., & Koenig, M. 1995, A&A, 300, 707
Tremaine, S., Gebhardt, K., Bender, R., et al. 2002, ApJ, 574, 740
Vestergaard, M., & Peterson, B. M. 2006, ApJ, 641, 689
Vestergaard, M., & Wilkes, B. J. 2001, ApJS, 134, 1
Wang, J.-G., Dong, X.-B., Wang, T.-G., et al. 2009, ApJ, 707, 1334
Wills, B. J., & Browne, I. W. A. 1986, ApJ, 302, 56
Woo, J.-H., Schulze, A., Park, D., et al. 2013, ApJ, 772, 49
Woo, J.-H., Treu, T., Barth, A. J., et al. 2010, ApJ, 716, 269